Review of Scientific Instruments

RESEARCH ARTICLE | MAY 12 2023

The Complex, Unique, and Powerful Imaging Instrument for Dynamics (CUPI²D) at the Spallation Neutron Source (invited)

Special Collection: New Science Opportunities at the Spallation Neutron Source Second Target Station

Adrian Brügger ; Hassina Z. Bilheux ; Jiao Y. Y. Lin ; George J. Nelson ; Andrew M. Kiss ; Jonathan Morris ; Matthew J. Connolly; Alexander M. Long ; Anton S. Tremsin ; Andrea Strzelec ; Mark H. Anderson ; Robert Agasie ; Charles E. A. Finney ; Martin L. Wissink ; Mija H. Hubler; Roland J.-M. Pellenq ; Claire E. White ; Brent J. Heuser ; Aaron E. Craft ; Jason M. Harp ; Chuting Tan ; Kathryn Morris ; Ann Junghans ; Sanna Sevanto ; Jeffrey M. Warren ; Fernando L. Esteban Florez ; Alexandru S. Biris; Maria Cekanova ; Nikolay Kardjilov ; Burkhard Schillinger ; Matthew J. Frost ; Sven C. Vogel

Rev. Sci. Instrum. 94, 051301 (2023)
https://doi.org/10.1063/5.0131778

Review of Scientific Instruments ARTICLE scitation.org/journal/rsi

The Complex, Unique, and Powerful Imaging Instrument for Dynamics (CUPI²D) at the Spallation Neutron Source (invited)

Cite as: Rev. Sci. Instrum. 94, 051301 (2023); doi: 10.1063/5.0131778
Submitted: 24 October 2022 • Accepted: 5 March 2023 •
Published Online: 12 May 2023

Adrian Brügger,[1] Hassina Z. Bilheux,[2,a)] Jiao Y. Y. Lin,[3] George J. Nelson,[4] Andrew M. Kiss,[5] Jonathan Morris,[6] Matthew J. Connolly,[7] Alexander M. Long,[8] Anton S. Tremsin,[9] Andrea Strzelec,[10] Mark H. Anderson,[10] Robert Agasie,[10] Charles E. A. Finney,[11] Martin L. Wissink,[11] Mija H. Hubler,[12] Roland J.-M. Pellenq,[13] Claire E. White,[14] Brent J. Heuser,[15] Aaron E. Craft,[16] Jason M. Harp,[17] Chuting Tan,[16] Kathryn Morris,[18] Ann Junghans,[19] Sanna Sevanto,[20] Jeffrey M. Warren,[21] Fernando L. Esteban Florez,[22] Alexandru S. Biris,[23] Maria Cekanova,[24] Nikolay Kardjilov,[25] Burkhard Schillinger,[26] Matthew J. Frost,[27] and Sven C. Vogel[8]

AFFILIATIONS

[1]Civil Engineering & Engineering Mechanics, Columbia University, New York, New York 10027, USA
[2]Oak Ridge National Laboratory, Spallation Neutron Source, Neutron Scattering Division, Oak Ridge, Tennessee 37831, USA
[3]Oak Ridge National Laboratory, Second Target Station Project, Oak Ridge, Tennessee 37831, USA
[4]Mechanical and Aerospace Engineering, University of Alabama-Huntsville, Huntsville, Alabama 35899, USA
[5]Brookhaven National Laboratory, National Synchrotron Light Source II, Photon Science Division, Upton, New York 11973, USA
[6]Physics, Xavier University, Cincinnati, Ohio 45207, USA
[7]Material Measurement Laboratory/Applied Chemicals and Materials Division, National Institute of Standards and Technology, Boulder, Colorado 80305, USA
[8]Los Alamos National Laboratory, Materials Science and Technology Division, Los Alamos, New Mexico 87545, USA
[9]Space Science Laboratory, University of California-Berkeley, Berkeley, California 94720, USA
[10]College of Engineering, University of Wisconsin-Madison, Madison, Wisconsin 53706, USA
[11]Oak Ridge National Laboratory, Buildings and Transportation Science Division, Oak Ridge, Tennessee 37831, USA
[12]College of Engineering and Applied Science, University of Colorado-Boulder, Boulder, Colorado 80309, USA
[13]International Research Laboratory, CNRS-George Washington University, Washington, District of Columbia 20052, USA
[14]Civil and Environmental Engineering, Princeton University, Princeton, New Jersey 08544, USA
[15]The Grainger College of Engineering, University of Illinois-Urbana Champaign, Urbana, Illinois 61801, USA
[16]Idaho National Laboratory, Characterization and Advanced Post-Irradiation Examination Division, Idaho Falls, Idaho 83415, USA
[17]Oak Ridge National Laboratory, Nuclear Energy and Fuel Cycle Division, Oak Ridge, Tennessee 37831, USA
[18]Biology, Xavier University, Cincinnati, Ohio 45207, USA
[19]Los Alamos National Laboratory, Nuclear Engineering and Nonproliferation Division, Los Alamos, New Mexico 87545, USA
[20]Los Alamos National Laboratory, Environmental Sciences Division, Los Alamos, New Mexico 87545, USA
[21]Oak Ridge National Laboratory, Environmental Sciences Division, Oak Ridge, Tennessee 37831, USA
[22]University of Oklahoma Health Sciences Center College of Dentistry, Oklahoma City, Oklahoma 73117, USA
[23]Center for Integrative Nanotechnology Sciences, University of Arkansas at Little Rock, Little Rock, Arkansas 72204, USA
[24]Integrity Laboratories, LLC, Knoxville, Tennessee 37932, USA
[25]Helmholtz-Zentrum-Berlin, Institute Applied Materials, Berlin 14109, Germany
[26]Physics, Technical University Munich, Garching 85748, Germany
[27]Oak Ridge National Laboratory, Neutron Technologies Division, Oak Ridge, Tennessee 37831, USA

Note: Paper published as part of the Special Topic on New Science Opportunities at the Spallation Neutron Source Second Target Station.
[a]**Author to whom correspondence should be addressed:** bilheuxhn@ornl.gov. **Telephone:** (+1) 865-574-0241

ABSTRACT

The Oak Ridge National Laboratory is planning to build the Second Target Station (STS) at the Spallation Neutron Source (SNS). STS will host a suite of novel instruments that complement the First Target Station's beamline capabilities by offering an increased flux for cold neutrons and a broader wavelength bandwidth. A novel neutron imaging beamline, named the Complex, Unique, and Powerful Imaging Instrument for Dynamics (CUPI^{2}D), is among the first eight instruments that will be commissioned at STS as part of the construction project. CUPI^{2}D is designed for a broad range of neutron imaging scientific applications, such as energy storage and conversion (batteries and fuel cells), materials science and engineering (additive manufacturing, superalloys, and archaeometry), nuclear materials (novel cladding materials, nuclear fuel, and moderators), cementitious materials, biology/medical/dental applications (regenerative medicine and cancer), and life sciences (plant–soil interactions and nutrient dynamics). The innovation of this instrument lies in the utilization of a high flux of wavelength-separated cold neutrons to perform *real time in situ* neutron grating interferometry and Bragg edge imaging—with a wavelength resolution of $\delta\lambda/\lambda \approx 0.3\%$—simultaneously when required, across a broad range of length and time scales. This manuscript briefly describes the science enabled at CUPI^{2}D based on its unique capabilities. The preliminary beamline performance, a design concept, and future development requirements are also presented.

 https://doi.org/10.1063/5.0131778

I. INTRODUCTION

Attenuation-based neutron radiography and computed tomography have contributed for decades to a broad range of scientific research applications at both continuous[1–8] and pulsed sources.[9–12] At research reactors and pulsed sources, research areas such as energy applications,[13–23] materials science,[24–29] engineering,[30–35] geosciences,[36–42] plant physiology,[43–52] archaeometry,[53–60] and medicine[61–64] have flourished over the past 20+ years. More recently, technological prowess in detector apparatus has demonstrated spatial resolution reaching a few μm.[65–67] Advanced techniques such as polarized neutron imaging[68–72] and neutron grating interferometry[73–80] have achieved new contrast mechanisms and detection sensitivity for features far below the pixel resolution by merging small angle scattering and neutron imaging. Pulsed sources provide a unique contrast mechanism based on the time-of-flight (TOF) information, i.e., the capability to determine the neutron's wavelength based on the TOF of the neutron. Novel wavelength-dependent techniques have enabled measurements of microstructure,[9,30,31,81–85] strain,[30,35,83,86–95] and elemental and/or isotopic content in materials,[96–103] such as engineered components and geomaterials. Over the past ten years, the interest generated by these novel TOF capabilities has led to the nascence of a new class of wavelength-dependent neutron imaging facilities at worldwide pulsed sources such as IMAT[12] at ISIS (Rutherford Appleton Laboratory) in the United Kingdom and RADEN[104] (Japanese Proton Accelerator Research Complex) in Japan; the development of dedicated capabilities at other facilities such as Los Alamos Neutron Science Center (LANSCE);[10] and the construction of VENUS (Versatile Neutron Imaging Instrument at SNS) at Oak Ridge National Laboratory in the United States,[105] ODIN at the European Spallation Neutron Source (ESS),[106,107] and ERNI at the Chinese Spallation Neutron Source (CSNS).[108]

The SNS is an accelerator-based pulsed neutron source that is outfitted with 19 state-of-the-art neutron scattering instruments optimized to mostly use thermal neutrons at its First Target Station (FTS) that are geared to provide unique capabilities across a broad range of scientific disciplines. Plans are underway to construct a Second Target Station (STS),[109] providing a high intensity beam of *cold* neutrons that will support complementary instruments, including one instrument optimized for TOF imaging. This beamline, named the Complex, Unique, and Powerful Imaging Instrument for Dynamics (CUPI^{2}D), will be equipped with the necessary optics and detectors to perform real time *in situ* Bragg edge imaging (BEI)[83] and neutron grating interferometry (nGI).[75,77,110] The combination of these capabilities and the high source intensity will allow for unprecedented fast measurements across a broad range of length and time scales currently unavailable at existing neutron imaging beamlines. CUPI^{2}D will be designed to complement the existing and future neutron imaging instruments at the Oak Ridge National Laboratory (ORNL): the HFIR CG-1D Multimodal Advanced Radiography Station (MARS)[111,112] and the Versatile Neutron Imaging Instrument at SNS (VENUS)[105] presently under construction with an anticipated completion date of summer 2024. MARS provides a high flux of cold neutrons and is being upgraded to provide both high spatial resolution imaging capabilities and white beam (i.e., wavelength-independent) neutron grating interferometry. VENUS is designed to offer a broad range of neutron wavelengths over a large fully illuminated field-of-view of 20×20 cm^2, with neutron energies ranging from epithermal to thermal, hence permitting the measurement of resonances and Bragg edges, respectively. The CUPI^{2}D imaging beamline will extend the range of materials and phenomena to be studied with the help of neutron imaging techniques. The cold neutron spectrum of the STS will extend the wavelength range beyond 10 Å needed for various studies, which require long data collection times at the existing flight paths due to the low flux at these wavelengths.

CUPI^{2}D encompasses a diverse scientific portfolio and will play a significant role in a broad range of scientific topics, including

materials science, energy (batteries, fuel cells, and nuclear), engineering, life sciences, biology, geosciences, medicine (cancer, biomaterials for scaffolds, and biofilm formation), dentistry (implants), and archaeometry.[8] Since CUPI^{2}D's capabilities permit fundamental science studies as well as applied research, the expected user base for the instrument will include researchers from academia, national laboratories, and industry. This paper briefly highlights a few scientific applications that will benefit from the future capabilities at CUPI^{2}D.

With a predicted *cold* neutron flux 20 times higher than that available at FTS VENUS[105] (see the discussion in the technical section), CUPI^{2}D will be designed to perform *real-time* investigations of *in situ* dynamic processes in advanced materials such as energy storage devices[113–115] and superalloys such as those utilized in aerospace,[84–86] under extreme environments generated by furnaces, load frames, pressure and gas cells, etc. Both the materials' phases and crystalline properties can be characterized using BEI, an atomic-level technique, as illustrated in Refs. 30, 83–85, 89, and 116. Briefly, the combination of BEI and nGI increases the probing length scale, from the atomic level to a few μm, with each technique providing enhanced contrast at a relevant scale. While BEI is sensitive to a material's phases and crystalline properties, nGI is based on scattering effects similar to small angle neutron scattering (SANS).[77] Most importantly, the instrument will enable the *simultaneous performance* of transmission imaging/tomography, BEI, and nGI, allowing us to quantify material and system kinetics at multiple length scales and at a time resolution ranging from seconds to a few minutes. CUPI^{2}D will be capable of associating several properties needed to be studied *in situ* and in *real time*, such as microporosity (nGI),[117–119] preferred microstructure orientation,[25] and strain (BEI)[84,86,88,94,120] in materials such as additively manufactured (AM) metals and other superalloys. The beamline will provide experimental data that, in turn, inform predictive models capable of anticipating stress-induced porosity changes and fracture evolution. CUPI^{2}D will contribute to the validation and scalability of AM components in failure-critical areas, such as aerospace parts and biomedical implants. The degradation and failure mechanisms in structures such as suspension bridges will be an opportune example of *in situ* experiments. Progress has been made on understanding the internal mechanics of multi-body wires in suspension bridges using neutron diffraction, but to date, it has not been possible to perform *spatially resolved live* and *in situ* imaging of degradation, overload, and plastic flow evolution of components (the latter of which can only be detected through imaging since plastic deformation mechanisms are independent of atomic lattice spacing resolved in diffraction).[121,122]

CUPI^{2}D will allow the imaging of full-size energy storage cells *in operando* over a full range of cycling conditions. The extension of conventional tomography to 4D (3D spatial and time) imaging capabilities will make available dynamic volumetric studies of the distribution and movement of light elements such as lithium and hydrogen in material components and in complete devices. While nGI focuses on mapping spatial non-uniformities in constituent materials and components, BEI measures the chemical phases in the functioning battery, as demonstrated in the literature.[113,114,123] Localized changes in material morphology, such as particle pulverization and changes in porous regions due to material expansion, will be observed with nGI. Localized state-of-charge, inhomogeneities, and other crystal structure changes that may arise during operation will be observed with BEI. Together, these capabilities will provide a multiscale understanding of the electrochemical processes in novel battery systems that will be transformational in developing new technologies in the field of energy storage.

Biological materials, such as plants, tissues, and microbes, are difficult to image using x-ray methods due to their low interaction with photons and potential for biological tissue damage. In addition, while neutrons have been successfully used to track water content and exchange between soils and roots,[36–52] it has been particularly difficult to image plant root–soil chemical interactions *in situ* due to their high water content. CUPI^{2}D will provide powerful new capabilities in "indirect" high resolution imaging using nGI of light elements [e.g., carbon (C), oxygen (O), nitrogen (N), and minerals], the basic building blocks of biological materials. This capability allows the *in situ* dynamic visualization of many natural phenomena that, to date, have been studied using other indirect methods. The BEI mode and nGI capabilities will allow the dynamic assessment of specific compounds (e.g., root nutrient uptake and root C release) and their interactions with water and soil surfaces to provide a map of crystalline phases (minerals) and porosity quantities. This research will revolutionize our understanding of plant/soil/water/nutrient/C relations and soil C sequestration capacity, leading to improved climate models and crop/land management strategies.

II. TECHNIQUES, CONCEPTUAL DESIGN, AND EXPECTED PERFORMANCE

A. Performance capabilities and equipment

CUPI^{2}D will be a multimodal, multi-length scale instrument capable of characterizing both natural and engineered materials, from the Å to the cm length scale at acquisition times ranging from seconds to minutes. These capabilities are achieved by providing BEI and nGI transformative capabilities simultaneously, as needed. Table I displays the source parameters, capability, and equipment requirements based on the instrument's anticipated scientific portfolio. The equipment requirements were collected from the scientific community during the competitive proposal process and are not necessarily explained throughout this section. Table I illustrates the types of capabilities required to successfully perform the proposed science, including detector technology and sample environment (SE). As such, this beamline's preliminary design will evolve with the advances in the various technical fields of study that will benefit CUPI^{2}D.

The desired performance capabilities will be achieved by selecting a moderator with the highest flux of cold neutrons, utilizing guides and advanced optical components while keeping the source-to-detector distance sufficient for a Bragg-edge resolution of $\delta\lambda/\lambda \approx 0.003$.[31,82,83,87,89,91,92,120,124]

B. Advantages of implementing Bragg edge imaging and neutron grating interferometry at pulsed sources

BEI is an ideal technique for a pulsed neutron source[30,125] since it focuses on measuring the abrupt changes in neutron transmission due to the crystalline structure or phase of the sample as a function of neutron wavelength (with a wavelength resolution on the order

TABLE I. Source parameters, key capabilities, and equipment requirements for the CUPI^{2}D beamline.

Parameter/equipment	Requirement(s)
Source power	0.7 MW
Source repetition rate	15 Hz
Choice of moderator	Cylinder
Variable moderator-to-detector distance	~21.5–22 to 34 m
Wavelength resolution ($\delta\lambda/\lambda$)	0.003
Spatial resolution	From 10 to 100 μm
λ_{min}	~2 Å
Beam transport	Elliptical guide system
Moderator-to-virtual-source distance	18 m
Maximum virtual-source-to-detector distance (L)	Variable and ~15 m
Collimation (L/D, D pinhole aperture size)	100 < L/D < 1000
Maximum field-of-view	15 × 15 cm^2
Advanced optics/equipment	Neutron grating interferometers, Wolter mirrors, polarization
Detectors	"Tileable" Micro-Channel Plate (MCP) Timepix4 (or newer generation) in TOF and centroiding modes simultaneously, event mode capability, charge coupled device (CCD), and/or scientific complementary metal–oxide–semiconductor (sCMOS)
Sample environment	Potentiostat, load frame for 2D kinetics, load frames for computed tomography (CT), inert gas furnace, −80 C biochamber, etc.
Computing capabilities	Servers at the beamline for fast guided machine learning acquisition/processing, visualization, and analysis

of $\delta\lambda/\lambda$ = 0.2%–0.5%). In fact, a sharp change in transmission occurs when the neutron wavelength, λ, is equal to twice the atomic spacing, *d*, for a specific <*hkl*> atomic plane. The height and position of the Bragg edge can provide phase and strain information, as illustrated in Refs. 27, 31, 81, 86, 89, 92, and 94. The combination of Bragg edge transmission with the small pixel size of an imaging detector is ideal for measuring phase/strain variations that would be averaged over a bulk measurement using, for example, diffraction.

The particle–wave duality of neutrons allows the measurement of a phase shift of a neutron beam due to the real part of an object's refraction index. Measurements of the neutron phase shift can be performed using a grating-induced coherent (in time and space) source of neutrons.[73,74] Materials such as titanium (Ti)- and nickel (Ni)-based superalloys have similar linear attenuation coefficients, and thus, an attenuation-based measurement cannot separate the two materials. However, their phase shifts are negative and positive, respectively, allowing them to be separated in 2D and 3D phase measurements. This technique is called Differential Phase Imaging (DPI), and the contrast comes from the refraction at interfaces between materials. Moreover, the grating interferometry system provides a high angular resolution that can be exploited to detect ultra-small-angle-scattering (USANS) effects. With this technique—called Dark Field Imaging (DFI)[35,78,79,126–128]—measurements of structures from nm to μm are possible, thus tremendously enhancing the imaging spatial information, which is not achievable when taking attenuation-based radiographs using conventional pinhole geometry systems. A parameter called the autocorrelation length, also known as the dark field length, is directly related to the microscopic sample structures that are being measured. Hence, by tuning the dark field length, ξ, one can probe through different length scales. ξ is given by $\xi = \lambda L_s/p_1$, where λ is the neutron wavelength, L_s is the sample-to-detector distance, and p_1 is the G_1 phase grating period. Commonly, neutron grating interferometers, such as the Talbot–Lau nGI system, are comprised of three gratings: G_0, the source grating; G_1, the phase grating; and G_2, the analyzer grating.[129] G_0 constructs the source coherence, while G_1 measures the phase/amplitude shift. G_2 is the absorption grating that is stepped perpendicularly to the beam to measure the intensity oscillations that are smaller than a pixel on the detector. Since p_1 is fixed, for a fixed wavelength, L_s must be increased to cover a significant correlation length range, leading to a decrease in image resolution that can be compensated using advanced neutron optics. This is not necessary at CUPI^{2}D since it will provide a broad range of neutron wavelengths simultaneously.

A conceptual design of a combined nGI/BEI setup is displayed in Fig. 1. The three gratings (G_0, G_1, and G_2) are placed close to the aperture such that the flux is maximized. The sample environment and micro-channel plate (MCP) Timepix (TPX) detector are moved upstream, accordingly. Since the source is pulsed and the MCP TPX is capable of timestamping neutrons as they arrive, BEI is effectively performed simultaneously by acquiring wavelength-resolved radiographs. All radiographs are acquired at the wavelength resolution required by BEI, which has the most stringent resolution requirement, and can be later binned into larger wavelength bins for nGI analysis.

C. Choice of moderator

CUPI^{2}D's prime directive is to provide the highest possible flux of wavelength-resolved cold neutrons—achievable only with STS's

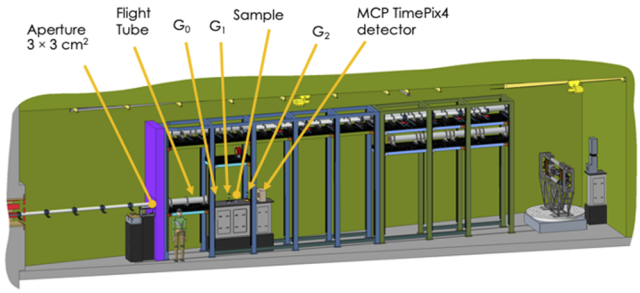

FIG. 1. Schematic of the neutron grating interferometer installed at CUPI^{2}D. When in place, the sample and detector are moved closer to the aperture, hence increasing the neutron flux on the sample. Since the source is pulsed and the MCP detector can timestamp neutrons, both nGI and BEI data can be acquired simultaneously. Neutrons enter the instrument from the left.

uniquely intense *cold* neutron flux—to perform both BEI and nGI with a sufficient temporal resolution to capture dynamic processes. Hence, wavelengths shorter than ~2 Å do not need to be propagated through the beamline path. The wavelength resolution is driven by BEI and should be on the order of $\delta\lambda/\lambda \approx 0.003$, as demonstrated in previous work.[31,82,83,87,89,91,92,120,124]

STS is designed to operate at 15 Hz, a lower repetition rate than FTS, which ensures broad wavelength bands. Two moderators are proposed for STS: (1) a cylinder moderator with a viewed area of 3 × 3 cm^2 that offers the best wavelength resolution (needed for BEI) and (2) a tube moderator with a 3 cm diameter viewing area and a comparatively higher flux than the cylinder moderator. While the tube moderator provides, on average, ~50% more neutrons, it produces a broader pulse than the cylinder moderator and, thus, a compromise in the wavelength resolution is made unless the instrument is much longer than on a cylinder moderator. The instrument would have to be longer than 50 m, as shown in Fig. 2,

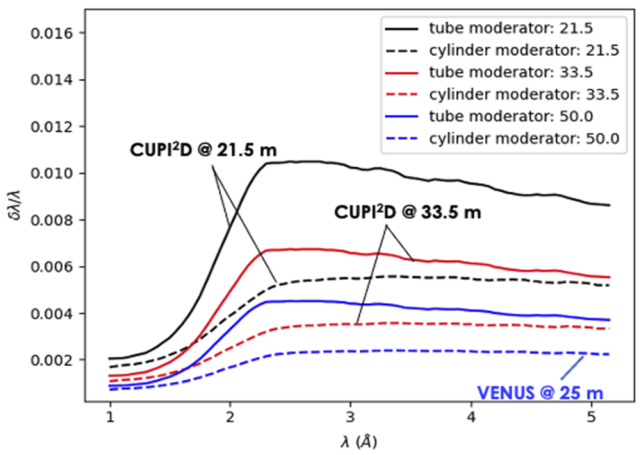

FIG. 2. Wavelength resolution as a function of neutron wavelength for the cylinder and tube moderators for the two extreme detector positions at CUPI^{2}D. As a comparison, for CUPI^{2}D to be comparable to VENUS, it would need to be at a distance of 50 m on a cylinder moderator and further downstream with a tube moderator (not displayed here). The legend values are provided in meters.

which illustrates the different wavelength resolutions achieved at both STS moderators for different source-to-detector distances. The overall frame width is inversely proportional to the moderator-to-detector distance, reducing the beamline's capability to measure fast kinetics over a broad range of wavelengths as the moderator-to-detector distance increases. Longer instruments also require longer guide systems, increasing the risk of unwanted inhomogeneities in the beam profile at the sample, resulting from misalignments and other imperfections (section gaps) in the guide system. The quality of the measured radiograph and potential neutron CT (nCT) reconstruction depends critically on the uniformity of the beam profile.

CUPI^{2}D is designed to have its most downstream detector position at ≈ 33.5 m, which corresponds to an overall wavelength band of $\Delta\lambda \approx 7.89$ Å and a wavelength resolution of $\delta\lambda/\lambda \approx 0.3\%$ on a cylinder moderator, matching the wavelength resolution requirements listed in the instrument specifications (Table I). This large instantaneous wavelength band is essential to the CUPI^{2}D scientific case, for example, to use Bragg edges to measure the chemical phases in batteries, which occur over several Å (from 3 Å to ≈ 12 Å), at cold wavelengths that are not available at VENUS due to the lack of flux beyond ≈ 5 Å. A narrow wavelength band, Δλ, would compromise the kinetic measurements of the same time event since not all appropriate wavelengths can be measured at the same time. Selecting a tube moderator jeopardizes the overall Δλ since $\delta\lambda/\lambda$ of 0.3% can only be achieved if the CUPI^{2}D imaging detector is placed at ≈ 54 m, thus corresponding to $\Delta\lambda \approx 4.89$ Å. Moreover, because the CUPI^{2}D detector can move as close as 21.5 m, the wavelength resolution on a tube moderator of $\delta\lambda/\lambda \approx 1\%$ (see Fig. 2) would be insufficient for BEI for materials science applications that require strain mapping with an accuracy of ≈100 με.[116,120,130] In comparison, VENUS's detector position is at 25 m, yielding a $\Delta\lambda \approx 2.64$ Å and $\delta\lambda/\lambda \approx 0.2\%$.

The simulated averaged brightness at CUPI^{2}D is expected to be at least 20 times higher than the VENUS's simulated brightness for neutron wavelengths higher than 2.5 Å, as illustrated in Fig. 3. Hence, CUPI^{2}D will be capable of achieving a much higher time

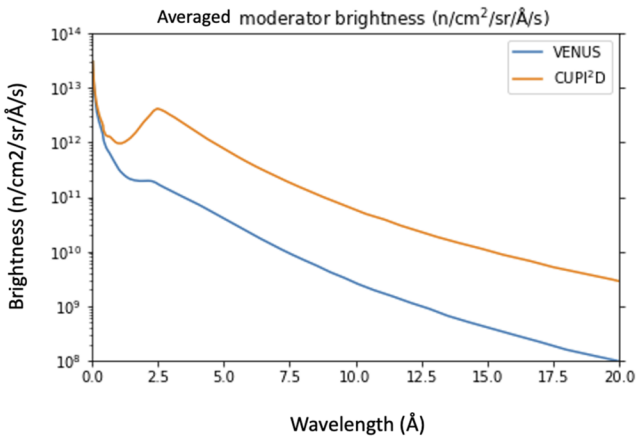

FIG. 3. Comparison of the simulated averaged brightness as a function of wavelength at CUPI^{2}D and VENUS.

resolution on the order of seconds to minutes, as compared to VENUS, which will require minutes to hours per measurement at similar cold neutron wavelengths.

D. Chopper optimization

Disk or bandwidth choppers are devices that prevent frame overlap between sequential pulses of neutrons. They act as mechanical bandpass filters and open to let only neutrons of the desired wavelength pass. Most FTS beamlines have three disk choppers to prevent frame overlap. Since the pulse frequency at STS is 15 Hz (4 times slower than FTS), fewer disk choppers are required. Since CUPI^{2}D has a variable moderator-to-detector distance, the disk choppers must allow different neutron wavelength frames, which can be realized by installing a double disk chopper with disks that spin in opposite directions, each with adjustable phases. Most of the beamline optics and components that produce background are installed in the bunker, with the double disk chopper installed at 6 m, followed by the T_0 chopper at 7.5 m. The T_0 chopper decreases the prompt gamma pulse and fast neutron intensities by several orders of magnitude. One double disk chopper is sufficient to stop the frame overlap of neutrons with wavelengths shorter than ~50 Å, as illustrated in Fig. 4.

E. Conceptual design of the instrument

Unlike FTS, the first 13.2 m (from the moderator) of an STS instrument is designed with common shielding called the bunker, which is shared by all beamlines located on the same side of the target building. This inevitably limits the floor space available to install imaging optics and introduces complexity in accessing the front-end area of the beamline in case of repair (several beamlines would need to be shut down to access CUPI^{2}D front-end optics). Thus, it is prudent to limit the CUPI^{2}D beamline components in the bunker to components that are *absolutely* necessary: the T_0 chopper, the frame-defining bandwidth choppers, and components that require heavy shielding, such as the beamline shutter, guides, beam collimators, and filters. These components are placed as far upstream as reasonable since they generate a significant background of neutrons and gammas that should be avoided close to the instrument cave. The STS moderator is bright but small (3×3 cm^2), which is amenable to "transporting" the neutron source to a downstream location named the "virtual source." For the abovementioned reasons, CUPI^{2}D is designed to create a virtual source 18 m away from the moderator using an elliptical guide system.

CUPI^{2}D can be divided into three main sections: (1) the bunker, shared by several instruments, starting at the source and ending at 13.2 m; (2) the instrument cave with a back wall at ~40 m; and (3) the radiological material area, the control hutch, and the user laboratory located directly behind the instrument. Figure 5 is a three-dimensional rendering of the beamline showing the bunker and cave sections and some of their respective aforementioned components.

The instrument cave is designed to allow space for implementing various mission-specific sample environments at the beamline. Complementary modalities are essential for short-lived phenomena such as those in the geosciences and plant systems. In fact, complementary nCT and x-ray computed tomography (xCT) have successfully been employed in many scientific fields, such as soil, batteries,[131] reservoir rocks,[132] and archaeological samples.[132,133] Magnetic Resonance Imaging (MRI) is another emerging capability that has recently been utilized to visualize plant rhizosphere in 3D.[134]

CUPI^{2}D's largest aperture matches the size of the virtual source and is located upstream of the instrument elevators. A variable aperture system can vary L/D ratios without moving the source-to-detector position (where L is the distance from the pinhole aperture, of diameter D, to the detector). CUPI^{2}D is designed for three *main* imaging modes, as displayed in Fig. 6. The high-intensity mode corresponds to the most upstream detector position at ~ 22 m (the original concept was 21.5 m) and, thus, corresponds to the lowest L/D of 100 and a maximum field of view (FOV) of ~ 4×4 cm^2, with a wavelength band of $\Delta\lambda \approx 12.3$ Å. The complementary mode

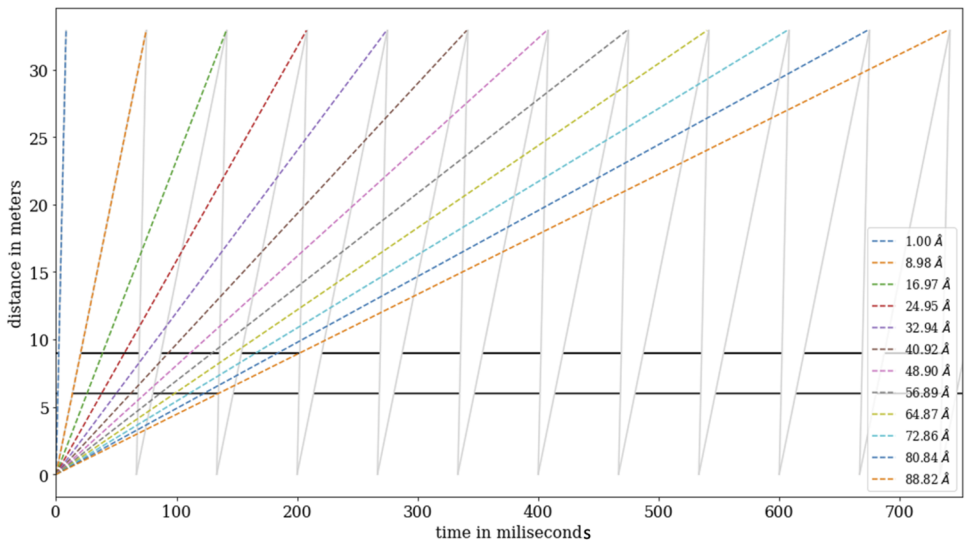

FIG. 4. Time diagram for the 15 Hz operations of the STS neutron source. The diagram shows neutrons emitted during the first frame (at time 0 s) and propagating through time and distance from the moderator. The black horizontal lines illustrate when the double disk chopper is closed. The oblique lines are color-coded for different neutron wavelengths. The 48.9 Å neutrons leak through the second frame. (For the purpose of these simulations, the second chopper at 9 m can be ignored.)

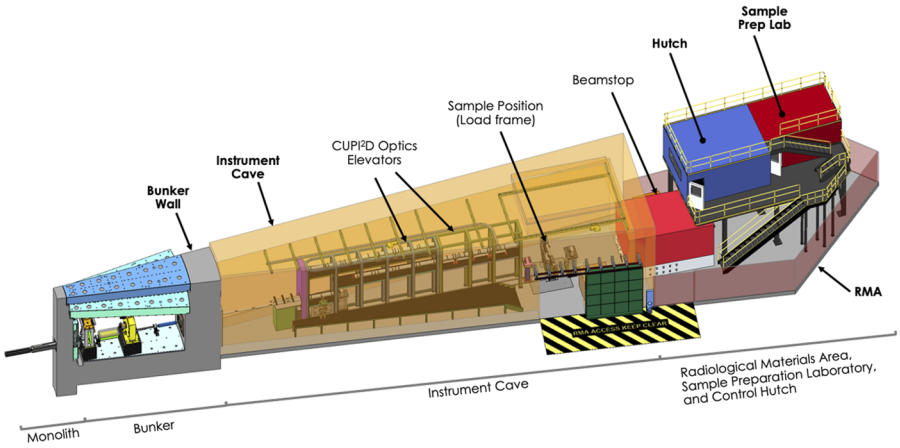

FIG. 5. Three-dimensional virtual rendering of the CUPI²D beamline showing the three main sections (bunker, cave, and RMA area) and some of their components.

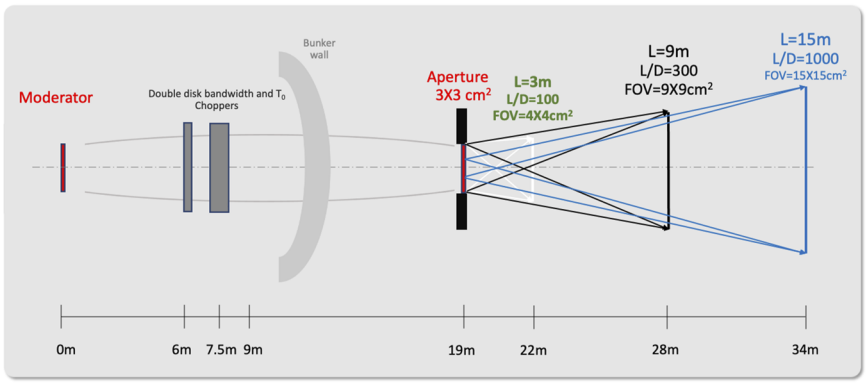

FIG. 6. Three main L/Ds and FOVs at CUPI²D: high flux, intermediate, and high wavelength-resolution modes, respectively, position 22, 28, and 34 m from the moderator.

is a high wavelength-resolution configuration with a detector positioned at ~ 34 m with the largest L/D of 1000 and a FOV of 15 × 15 cm^2 and a wavelength band of $\Delta\lambda \approx 7.89$ Å. Finally, the intermediate mode at 28 m, with a FOV of 9 × 9 cm^2 and an L/D of 300, allows for a balance between intensity, FOV, and wavelength resolution. Advanced optics, such as Wolter mirrors, gratings, and polarization, are installed on elevators similar to the current elevator system at the RADEN imaging beamline at J-PARC,[104] which is equipped with interchangeable optics, grating interferometers, polarization, and flight tubes. The installation of these optics on elevators (Fig. 5) allows for swift configuration changes between detector positions and imaging modalities (e.g., nGI may be used for selected measurements only, as it sacrifices flux).

To maximize the neutron flux, a straight, elliptical guide system is adopted to transport the source from the moderator and focuses on the virtual source aperture position at 18 m. The elliptical neutron transport system consists of two half-ellipses that are the left and right halves of two nearly identical ellipses: both are centered at around z = 9 m. Both ellipses have their first focal points slightly before the moderator and their second focal points slightly behind the aperture. Such a design provides the phase space (3 cm in height and width and an ~0.7° divergence) required for the three L/D collimation settings illustrated in white, black, and blue in Fig. 6. To estimate the performance of the optical design, simulations were performed by combining MCViNE[135,136] and McStas[137–139] simulation scripts to estimate the performance of the optical design. As a representative example, the performance of the neutron transport for L/D = 100 is presented in Fig. 7. Nearly 90% of the source brilliance is transferred for neutrons with wavelengths longer than 2.5 Å. The maximum flux is about 4 × 10^8 neutrons per second per cm^2 per Å at λ = 2.5 Å.

These initial simulations have yielded homogeneous intensity distributions within the desired field of view for all three modes. Figure 8 (top) shows the two-dimensional intensity patterns integrated over 1–9 Å at z = 22 m, z = 28 m, and z = 34 m detector positions for L/D = 100, 300, and 1000, respectively. In the case of L/D = 100, the FOV is limited by a region that comprises all pixels with an intensity that is > 90% of the maximum intensity (at the center). In the cases of L/D = 300 and 1000, the FOV is 9 × 9 and 15 × 15 cm^2, respectively. Further simulations and optimization are underway to account for the gaps introduced by the T_0 and double disk bandwidth choppers, to be reported elsewhere.

As illustrated in Fig. 8 (bottom), the modes corresponding to L/D = 300 and 1000 display less structure within the FOV than the simulation at L/D = 100 because they allow narrower neutron trajectories, i.e., those with a lower divergence through the aperture. As the detector moves closer to the variable aperture system, it can see neutrons with more reflections and a higher divergence.

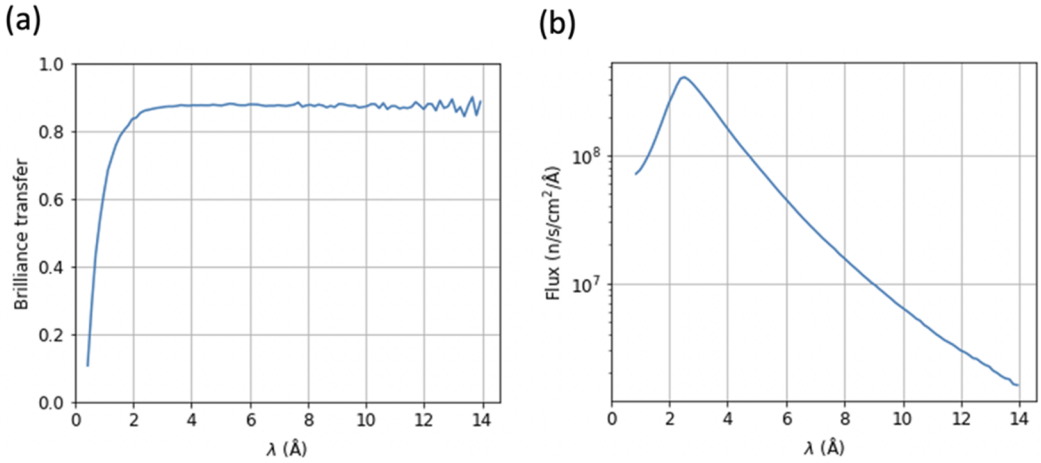

FIG. 7. Performance of the neutron elliptical transport system of the CUPI^{2}D conceptual design for L/D = 100. (a) Brilliance transfer as a function of neutron wavelength. (b) Neutron flux as a function of wavelength.

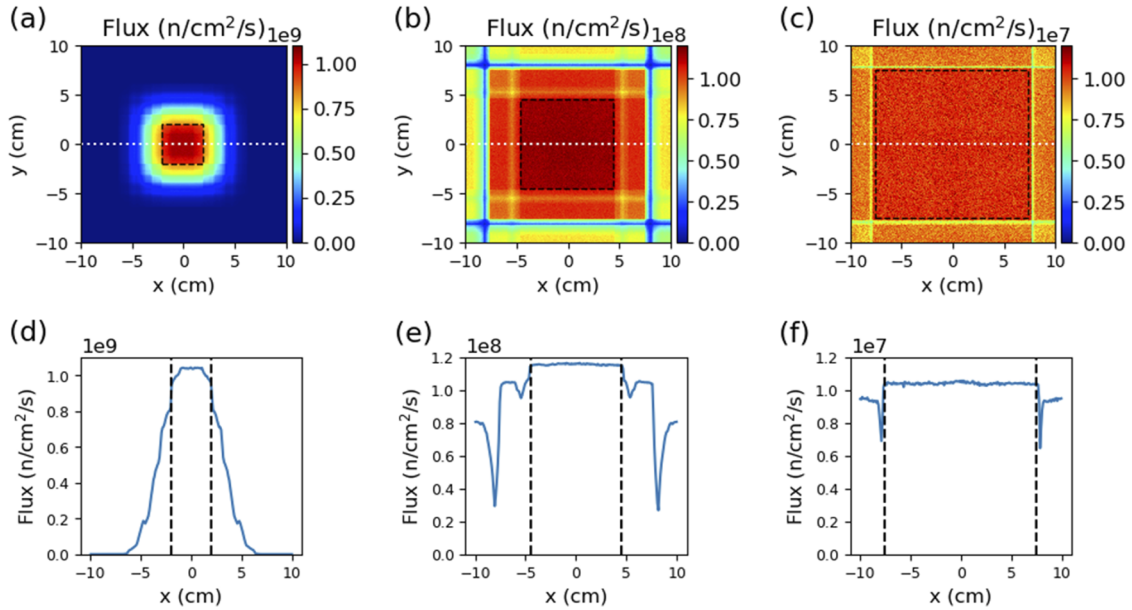

FIG. 8. Top: simulated radiographs and FOVs for L/Ds (a) 100, (b) 300, and (c) 1000, respectively, in the absence of a sample. The FOVs are indicated with the dashed black boxes. Intensities are homogeneous across the FOV for L/D = 300 and 1000. For L/D = 100, the intensity drops gradually by 10% from the inner region to the outer region within the FOV. Bottom: neutron flux profiles at the vertical center of the radiograph for L/Ds (d) 100, (e) 300, and (f) 1000 along the horizontal direction [see the corresponding white dotted lines in the radiographs (a), (b), and (c)]. FOVs are indicated with the two vertical dashed lines in (d), (e), and (f).

III. SUMMARY

The future CUPI^{2}D imaging beamline will broaden the science portfolio of the neutron imaging program at Oak Ridge National Laboratory by enabling material characterization across broad length and time scales. CUPI^{2}D will have a transformational impact on scientific areas such as energy storage and conversion (batteries, fuel cells to transform energy, and transportation fields), materials engineering (additive manufacturing and superalloys), nuclear materials (novel fuel cladding and moderators), cementitious materials, biology, and ecosystems (*in situ* soil–plant fluid/nutrient dynamics), and medical/dental applications (3D printed adaptive implants). The broad and diverse science portfolio is inherently concomitant with a wide-ranging sample environment.

The innovation of this instrument lies in the utilization of a high flux of cold neutrons for performing *real time in situ* neutron grating interferometry and Bragg edge imaging, with a wave-

length resolution of $\delta\lambda/\lambda \approx 0.3\%$, simultaneously when required, across a broad range of length and time scales. The proposed timeline for the construction of the STS and CUPI^{2}D is 10–15 years from today. There are three main modes at CUPI^{2}D that correspond to three different L/Ds, FOVs, wavelength resolutions, and fluxes at each position. These are called high flux (L/D 100, closest), intermediate (L/D 300), and high wavelength resolution (L/D 1000, farthest). Advanced optics such as Wolter mirrors are being considered at CUPI^{2}D. Further optimization of the beamline concept is underway and will be published in a future article.

ACKNOWLEDGMENTS

A portion of this research used resources at the Spallation Neutron Source, a DOE Office of Science User Facility operated by the Oak Ridge National Laboratory. This research used resources of the Spallation Neutron Source Second Target Station Project at Oak Ridge National Laboratory (ORNL). ORNL is managed by UT-Battelle, LLC, for DOE's Office of Science, the single largest supporter of basic research in the physical sciences in the United States. This material was based upon the work supported by the US Department of Energy, Office of Science, Office of Biological and Environmental Research. This work was also supported by the US Department of Energy (DOE), Office of Energy Efficiency and Renewable Energy, Bioenergy Technologies Office via the Systems Development and Integration program, and the US Department of Energy, Office of Energy Efficiency and Renewable Energy, Vehicle Technologies Office via the Advanced Combustion Engine Systems program. This research was supported by the DOE Office of Fossil Energy and Carbon Management. This work was also supported by Los Alamos National Laboratory LDRD Project No. 20200109DR.

The authors would like to thank Dr. Ken Andersen, Dr. Ken Herwig, Mrs. Cristina Boone, Mr. Scott Dixon, and Mr. William (Bill) Turner for their invaluable contributions to the concept and engineering design of the CUPI^{2}D beamline. The team would also like to thank colleagues at ORNL for brainstorming discussions about CUPI^{2}D: Dr. Yuxuan Zhang, Dr. Jean-Christophe Bilheux, and Mr. Erik Stringfellow. A special thank you to Dr. Franz Gallmeier for providing the source terms for the VENUS and CUPI^{2}D beamlines. The authors would also like to thank Mr. Harley Skorpenske for sharing his expertise in many fruitful discussions on the implementation of *in situ* load frames and furnaces in neutron diffraction and their potential implementation on an imaging beamline.

This manuscript has been authored by UT-Battelle, LLC, under Contract No. DE-AC05-00OR22725 with the US Department of Energy (DOE). The US government retains and the publisher, by accepting the article for publication, acknowledges that the US government retains a nonexclusive, paid-up, irrevocable, worldwide license to publish or reproduce the published form of this manuscript, or allow others to do so, for US government purposes. DOE will provide public access to these results of federally sponsored research in accordance with the DOE Public Access Plan (http://energy.gov/downloads/doe-public-access-plan).

AUTHOR DECLARATIONS

Conflict of Interest

The authors have no conflicts to disclose.

Author Contributions

Adrian Brügger: Conceptualization (supporting); Project administration (supporting); Writing – original draft (equal); Writing – review & editing (equal). **Hassina Z. Bilheux**: Conceptualization (lead); Project administration (lead); Writing – original draft (lead); Writing – review & editing (lead). **Jiao Y. Y. Lin**: Conceptualization (lead); Writing – original draft (supporting); Writing – review & editing (supporting). **George J. Nelson**: Conceptualization (supporting); Writing – original draft (supporting). **Andrew M. Kiss**: Writing – original draft (supporting). **Jonathan Morris**: Writing – original draft (supporting); Writing – review & editing (supporting). **Matthew J. Connolly**: Writing – original draft (supporting); Writing – review & editing (supporting). **Alexander M. Long**: Writing – original draft (supporting). **Anton S. Tremsin**: Conceptualization (supporting); Writing – original draft (supporting). **Andrea Strzelec**: Writing – original draft (supporting). **Mark H. Anderson**: Writing – original draft (supporting). **Robert Agasie**: Writing – original draft (supporting). **Charles E. A. Finney**: Writing – original draft (supporting). **Martin L. Wissink**: Writing – original draft (supporting). **Mija H. Hubler**: Writing – original draft (supporting). **Roland J.-M. Pellenq**: Writing – original draft (supporting). **Claire E. White**: Writing – original draft (supporting); Writing – review & editing (supporting). **Brent J. Heuser**: Writing – original draft (supporting). **Aaron E. Craft**: Writing – original draft (supporting). **Jason M. Harp**: Writing – original draft (supporting). **Chuting Tan**; Writing – original draft (supporting). **Kathryn Morris**: Writing – original draft (supporting); Writing – review & editing (supporting). **Ann Junghans**: Writing – original draft (supporting). **Sanna Sevanto**: Writing – original draft (supporting). **Jeffrey M. Warren**: Writing – original draft (supporting); Writing – review & editing (supporting). **Fernando L. Esteban Florez**: Writing – original draft (supporting); Writing – review & editing (supporting). **Alexandru S. Biris**: Writing – original draft (supporting). **Maria Cekanova**: Writing – original draft (supporting); Writing – review & editing (supporting). **Nikolay Kardjilov**: Writing – original draft (supporting); Writing – review & editing (supporting). **Burkhard Schillinger**; Writing – original draft (supporting); Writing – review & editing (supporting). **Matthew J. Frost**: Writing – original draft (supporting). **Sven C. Voge**: Writing – original draft (supporting); Writing – review & editing (supporting).

DATA AVAILABILITY

Data sharing is not applicable to this article as no new data were created or analyzed in this study.

REFERENCES

[1] B. Schillinger *et al.*, "The design of the neutron radiography and tomography facility at the new research reactor FRM-II at Technical University Munich," Appl. Radiat. Isot. **61**(4), 653–657 (2004).

[2]G. Kühne *et al.*, "CNR—The new beamline for cold neutron imaging at the Swiss spallation neutron source SINQ," Nucl. Instrum. Methods Phys. Res., Sect. A **542**(1-3), 264–270 (2005).
[3]D. S. Hussey *et al.*, "A new cold neutron imaging instrument at NIST," Phys. Procedia **69**, 48–54 (2015).
[4]A. Tengattini *et al.*, "NeXT-grenoble, the neutron and X-ray tomograph in Grenoble," Nucl. Instrum. Methods Phys. Res., Sect. A **968**, 163939 (2020).
[5]F. Salvemini *et al.*, "DINGO–the neutron imaging station at ANSTO: Embracing material science, palaeontology, and cultural heritage," Neutron News **27**(2), 14–19 (2016).
[6]N. Kardjilov, A. Hilger, and I. Manke, "CONRAD-2: Cold neutron tomography and radiography at BER II (V7)," J. Large-Scale Res. Facil. **2**, A98 (2016).
[7]D. Jacobson *et al.*, Neutron imaging facility at BT-2 and tomography of fuel cells. AND OPPORTUNITIES (2006).
[8]I. S. Anderson, R. L. McGreevy, and H. Z. Bilheux, *Neutron Imaging and Applications* (Springer Science+ Business Media, 2009), Vol. 200, pp. 987–990.
[9]W. Kockelmann *et al.*, "Energy-selective neutron transmission imaging at a pulsed source," Nucl. Instrum. Methods Phys. Res., Sect. A **578**(2), 421–434 (2007).
[10]R. Nelson *et al.*, "Neutron imaging at LANSCE—from cold to ultrafast," J. Imag. **4**(2), 45 (2018).
[11]T. Shinohara and T. Kai, "Commissioning start of energy-resolved neutron imaging system, RADEN in J-PARC," Neutron News **26**(2), 11–14 (2015).
[12]W. Kockelmann *et al.*, "Time-of-flight neutron imaging on IMAT@ISIS: A new user facility for materials science," J. Imag. **4**(3), 47 (2018).
[13]B. Michalak *et al.*, "Gas evolution in operating lithium-ion batteries studied in situ by neutron imaging," Sci. Rep. **5**, 15627 (2015).
[14]J. Nanda *et al.*, "Anomalous discharge product distribution in lithium-air cathodes," J. Phys. Chem. C **116**(15), 8401–8408 (2012).
[15]J. Nanda *et al.*, "Multiscale neutron and X-ray tomographic studies on high capacity lithium battery chemistries," Abstr. Papers Am Chem. Soc., **MA2014-02** 248 (2014).
[16]H. Zhou *et al.*, "Probing multiscale transport and inhomogeneity in a lithium-ion pouch cell using in situ neutron methods," ACS Energy Lett. **1**(5), 981–986 (2016).
[17]Z. Nie *et al.*, "Probing lithiation and delithiation of thick sintered lithium-ion battery electrodes with neutron imaging," J. Power Sources **419**, 127–136 (2019).
[18]J. P. Owejan *et al.*, "In situ investigation of water transport in an operating PEM fuel cell using neutron radiography: Part 2—Transient water accumulation in an interdigitated cathode flow field," Int. J. Heat Mass Transfer **49**(25-26), 4721–4731 (2006).
[19]D. S. Hussey *et al.*, "Neutron images of the through-plane water distribution of an operating PEM fuel cell," J. Power Sources **172**(1), 225–228 (2007).
[20]D. S. Hussey *et al.*, "In situ fuel cell water metrology at the NIST neutron imaging facility," J. Fuel Cell Sci. Technol. **7**(2), 021024 (2010).
[21]C. Tötzke *et al.*, "Large area high resolution neutron imaging detector for fuel cell research," J. Power Sources **196**(10), 4631–4637 (2011).
[22]R. F. Ziesche *et al.*, "4D imaging of lithium-batteries using correlative neutron and X-ray tomography with a virtual unrolling technique," Nat Commun **11**(1), 777 (2020).
[23]R. F. Ziesche *et al.*, "Neutron imaging of lithium batteries," Joule **6**(1), 35–52 (2022).
[24]H. Bilheux, "Neutron characterization of additively manufactured inconel 718," Adv. Mater. Process. **174**(8), 16–20 (2016).
[25]R. R. Dehoff *et al.*, "Site specific control of crystallographic grain orientation through electron beam additive manufacturing," Mater. Sci. Technol. **31**(8), 931–938 (2015).
[26]T. Smith *et al.*, "High resolution neutron radiography and tomography of hydrided zircaloy-4 cladding materials," in *Proceedings of the 10th World Conference on Neutron Radiography (Wcnr-10)*, 2015, pp. 478–482.
[27]H. Sato *et al.*, "Relation between Vickers Hardness and Bragg-Edge broadening in quenched steel rods observed by pulsed neutron transmission imaging," Mater. Trans. **56**(8), 1147–1152 (2015).
[28]E. E. Looney *et al.*, "Ex situ and in situ neutron imaging of enzymatic electrochemical cells," Electrochim. Acta **213**, 244–251 (2016).
[29]R. S. Longchamps *et al.*, "Neutron imaging and electrochemical characterization of a glucose oxidase-based enzymatic electrochemical cell," J. Electrochem. Energy Convers. Storage **15**(1), 011007 (2018).
[30]J. R. Santisteban *et al.*, "Engineering applications of Bragg-edge neutron transmission," Appl. Phys. A: Mater. Sci. Process. **74**, s1433–s1436 (2002).
[31]R. Woracek *et al.*, "3D mapping of crystallographic phase distribution using energy-selective neutron tomography," Adv. Mater. **26**(24), 4069–4073 (2014).
[32]J. Brunner *et al.*, "Dynamic neutron radiography of a combustion engine," in *Proceedings of 7th World Conference on Neutron Radiography* (Citeseer, Rome, 2002).
[33]A. S. Losko *et al.*, "Separation of uptake of water and ions in porous materials using energy resolved neutron imaging," JOM **72**(9), 3288–3295 (2020).
[34]P. Zhang *et al.*, "Application of neutron imaging to investigate fundamental aspects of durability of cement-based materials: A review," Cem. Concr. Res. **108**, 152–166 (2018).
[35]M. Bacak *et al.*, "Neutron dark-field imaging applied to porosity and deformation-induced phase transitions in additively manufactured steels," Mater. Des. **195**, 109009 (2020).
[36]J. W. Brabazon *et al.*, "Rock fracture sorptivity as related to aperture width and surface roughness," Vadose Zone J. **18**(1), 1–10 (2019).
[37]C.-L. Cheng *et al.*, "Rapid imbibition of water in fractures within unsaturated sedimentary rock," Adv. Water Resour. **77**, 82–89 (2015).
[38]C. L. Cheng *et al.*, "Average soil water retention curves measured by neutron radiography," Soil Sci. Soc. Am. J. **76**(4), 1184–1191 (2012).
[39]V. H. DiStefano *et al.*, "Spontaneous imbibition of water and determination of effective contact angles in the Eagle Ford Shale Formation using neutron imaging," J. Earth Sci. **28**(5), 874–887 (2017).
[40]B. B. Horodecky *et al.*, "Onset dynamics of air-water menisci on rock fracture surfaces," Adv. Water Resour. **146**, 103754 (2020).
[41]M. Kang *et al.*, "Diffusivity and sorptivity of Berea sandstone determined using neutron radiography," Vadose Zone J. **12**(3), 1–8 (2013).
[42]E. Perfect *et al.*, "Neutron imaging of hydrogen-rich fluids in geomaterials and engineered porous media: A review," Earth-Sci. Rev. **129**, 120–135 (2014).
[43]I. Dhiman *et al.*, "Quantifying root water extraction after drought recovery using sub-mm in situ empirical data," Plant Soil **424**(1-2), 73–89 (2017).
[44]J. M. Warren *et al.*, "Neutron imaging reveals internal plant water dynamics," Plant Soil **366**(1-2), 683–693 (2013).
[45]H. Z. Bilheux *et al.*, "Neutron imaging of fluids in plant-soil-rock systems using the ORNL/HFIR CG-1 beamline," Geochim. Cosmochim. Acta **74**(12), A91 (2010).
[46]A. Carminati *et al.*, "Dynamics of soil water content in the rhizosphere," Plant Soil **332**(1-2), 163–176 (2010).
[47]H. G. Esser *et al.*, "Neutron radiography and tomography of water distribution in the root zone," J. Plant Nutr. Soil Sci. **173**(5), 757–764 (2010).
[48]M. Holz *et al.*, "Rhizodeposition under drought is controlled by root growth rate and rhizosphere water content," Plant Soil **423**(1-2), 429–442 (2017).
[49]S. D. Keyes *et al.*, "High resolution synchrotron imaging of wheat root hairs growing in soil and image based modelling of phosphate uptake," New Phytol. **198**(4), 1023–1029 (2013).
[50]A. B. Moradi *et al.*, "Three-dimensional visualization and quantification of water content in the rhizosphere," New Phytol. **192**(3), 653–663 (2011).
[51]C. Totzke *et al.*, "Capturing 3D water flow in rooted soil by ultra-fast neutron tomography," Sci. Rep. **7**(1), 6192 (2017).
[52]M. W. Malone *et al.*, "In vivo observation of tree drought response with low-field NMR and neutron imaging," Front. Plant Sci. **7**, 564 (2016).
[53]S. Caporali *et al.*, "Structural characterization of iron meteorites through neutron tomography," Minerals **6**(1), 14 (2016).
[54]M. Griesser *et al.*, "Application of X-ray and neutron tomography to study antique Greek bronze coins with a high lead content," IOP Conf. Ser.: Mater. Sci. Eng. **37**, 012011 (2012).
[55]A. A. Kaloyan *et al.*, "Synchrotron and neutron tomography for the investigation of paleontological objects," J. Surf. Invest.: X-Ray, Synchrotron Neutron Tech. **8**(6), 1093–1099 (2014).

[56]F. Salvemini *et al.*, "Neutron tomographic analysis: Material characterization of silver and electrum coins from the 6th and 5th centuries BCE," Mater. Characteriz. **118**, 175–185 (2016).
[57]I. Fierascu *et al.*, "Analytical methods based on ionizing radiation for the non-destructive analysis of cultural heritage objects," in *Advanced Topics in Optoelectronics, Microelectronics, and Nanotechnologies IX*, 10977 (SPIE, 2018), pp. 256–260.
[58]S. N. Herringer *et al.*, "Quantification of water absorption and transport in parchment," in *Proceedings of the 10th World Conference on Neutron Radiography (Wcnr-10)*, 2015, pp. 524–529.
[59]S. N. Herringer *et al.*, "Evaluation of segregation in Roman sestertius coins," J. Mater. Sci. **53**(3), 2161–2170 (2017).
[60]K. Ryzewski *et al.*, "Neutron imaging of archaeological bronzes at the Oak Ridge national laboratory," in 7th International Topical Meeting on Neutron Radiography (Itmnr-7), 2013, Vol. 43, pp. 343–351.
[61]M. Cekanova *et al.*, "Neutron imaging: Detection of cancer using animal model," in *Proceedings of the 2014 Biomedical Sciences and Engineering Conference* (IEEE, 2014).
[62]H. Bilheux *et al.*, "Multi-scale applications of neutron scattering and imaging," in *Proceedings of the 2014 Biomedical Sciences and Engineering Conference* (IEEE, 2014).
[63]H. Z. Bilheux *et al.*, "Neutron imaging at the Oak Ridge National laboratory: Application to biological research," in *Proceedings of the 2014 Biomedical Sciences and Engineering Conference* (IEEE, 2014).
[64]H. Z. Bilheux *et al.*, "Neutron radiography and computed tomography of biological systems at the Oak Ridge National Laboratory's high flux isotope reactor," J. Vis. Exp. **171**, e61688 (2021).
[65]M. Morgano *et al.*, "Unlocking high spatial resolution in neutron imaging through an add-on fibre optics taper," Opt. Express **26**(2), 1809–1816 (2018).
[66]P. Trtik *et al.*, "Improving the spatial resolution of neutron imaging at Paul Scherrer Institut—The neutron microscope project," Phys. Procedia **69**, 169–176 (2015).
[67]P. Trtik and E. H. Lehmann, "Progress in High-resolution neutron imaging at the Paul Scherrer Institut - the neutron microscope project," J. Phys.: Conf. Ser. **746**, 012004 (2016).
[68]M. Dawson *et al.*, "Polarized neutron imaging using helium-3 cells and a polychromatic beam," Nucl. Instrum. Methods Phys. Res., Sect. A **651**(1), 140–144 (2011).
[69]M. Dawson *et al.*, "Imaging with polarized neutrons," New J. Phys. **11**(4), 23 (2009).
[70]N. Kardjilov *et al.*, "Three-dimensional imaging of magnetic fields with polarized neutrons," Nat. Phys. **4**(5), 399–403 (2008).
[71]I. Manke *et al.*, "Polarized neutron imaging at the CONRAD instrument at Helmholtz Centre Berlin," Nucl. Instrum. Methods Phys. Res., Sect. A **605**(1-2), 26–29 (2009).
[72]W. Treimer, "Radiography and tomography with polarized neutrons," J. Magn. Magn. Mater. **350**, 188–198 (2014).
[73]N. Kardjilov *et al.*, "Improving the image contrast and resolution in the phase-contrast neutron radiography," Nucl. Instrum. Methods Phys. Res., Sect. A **542** (1-3), 100–105 (2005).
[74]E. Lehmann *et al.*, "Non-destructive testing with neutron phase contrast imaging," Nucl. Instrum. Methods Phys. Res., Sect. A **542**(1-3), 95–99 (2005).
[75]F. Pfeiffer *et al.*, "Neutron phase imaging and tomography," Phys. Rev. Lett. **96**(21), 215505 (2006).
[76]T. Reimann *et al.*, "The new neutron grating interferometer at the ANTARES beamline: Design, principles and applications," J. Appl. Crystallogr. **49**(5), 1488–1500 (2016).
[77]M. Strobl, "General solution for quantitative dark-field contrast imaging with grating interferometers," Sci. Rep. **4**, 7243 (2014).
[78]M. Strobl *et al.*, "Wavelength-dispersive dark-field contrast: Micrometre structure resolution in neutron imaging with gratings," J. Appl. Crystallogr. **49**(2), 569–573 (2016).
[79]M. Strobl *et al.*, "Differential phase contrast and dark field neutron imaging," Nucl. Instrum. Methods Phys. Res., Sect. A **605**(1-2), 9–12 (2009).
[80]M. Strobl *et al.*, "Quantitative neutron dark-field imaging through spin-echo interferometry," Sci. Rep. **5**, 16576 (2015).
[81]L. L. Dessieux, A. D. Stoica, and P. R. Bingham, "Single crystal to polycrystal neutron transmission simulation," Rev. Sci. Instrum. **89**(2), 025103 (2018).
[82]E. H. Lehmann *et al.*, "Energy-selective neutron imaging with high spatial resolution and its impact on the study of crystalline-structured materials," Nucl. Instrum. Methods Phys. Res., Sect. A **735**, 102–109 (2014).
[83]R. Woracek *et al.*, "Diffraction in neutron imaging—A review," Nucl. Instrum. Methods Phys. Res., Sect. A **878**, 141–158 (2018).
[84]G. Song *et al.*, "Characterization of crystallographic structures using Bragg-Edge neutron imaging at the Spallation Neutron Source," J. Imag. **3**(4), 65 (2017).
[85]Q. Xie *et al.*, "Applying neutron transmission physics and 3D statistical full-field model to understand 2D Bragg-edge imaging," J. Appl. Phys. **123**(7), 074901 (2018).
[86]A. S. Tremsin *et al.*, "Monitoring residual strain relaxation and preferred grain orientation of additively manufactured Inconel 625 by in-situ neutron imaging," Addit. Manuf. **46**, 102130 (2021).
[87]K. Oikawa *et al.*, "Recent progress on practical materials study by Bragg edge imaging at J-PARC," Physica B **551**, 436–442 (2018).
[88]R. S. Ramadhan *et al.*, "Characterization and application of Bragg-edge transmission imaging for strain measurement and crystallographic analysis on the IMAT beamline," J. Appl. Crystallogr. **52**(2), 351–368 (2019).
[89]A. Tremsin *et al.*, "Energy-resolved neutron imaging for reconstruction of strain introduced by cold working," J. Imag. **4**(3), 48 (2018).
[90]A. S. Tremsin *et al.*, "Investigation of microstructure in additive manufactured Inconel 625 by spatially resolved neutron transmission spectroscopy," Sci. Technol. Adv. Mater. **17**(1), 324–336 (2016).
[91]A. S. Tremsin *et al.*, "Transmission Bragg edge spectroscopy measurements at ORNL Spallation Neutron Source," J. Phys.: Conf. Ser. **251**(1), 012069 (2010).
[92]A. S. Tremsin *et al.*, "High-resolution strain mapping through time-of-flight neutron transmission diffraction," Mater. Sci. Forum **772**, 9–13 (2013).
[93]A. S. Tremsin *et al.*, "Energy-resolved neutron imaging options at a small angle neutron scattering instrument at the Australian Center for Neutron Scattering," Rev. Sci. Instrum. **90**(3), 035114 (2019).
[94]R. Woracek *et al.*, "Neutron Bragg-edge-imaging for strain mapping under *in situ* tensile loading," J. Appl. Phys. **109**(9), 093506 (2011).
[95]J. N. Hendriks *et al.*, "Bragg-edge elastic strain tomography for in situ systems from energy-resolved neutron transmission imaging," Phys. Rev. Mater. **1**(5), 053802 (2017).
[96]M. Ooi *et al.*, "Neutron resonance imaging of a Au-In-Cd alloy for the JSNS," in 7th International Topical Meeting on Neutron Radiography (Itmnr-7), 2013, Vol. 43, pp. 337–342.
[97]A. S. Tremsin *et al.*, "Spatially resolved remote measurement of temperature by neutron resonance absorption," Nucl. Instrum. Methods Phys. Res., Sect. A **803**, 15–23 (2015).
[98]A. S. Tremsin *et al.*, "High resolution neutron resonance absorption imaging at a pulsed neutron beamline," in *2011 IEEE Nuclear Science Symposium and Medical Imaging Conference (NSS/MIC)* (IEEE, 2011), pp. 1501–1505.
[99]A. S. Tremsin *et al.*, "High resolution neutron resonance absorption imaging at a pulsed neutron beamline," IEEE Trans. Nucl. Sci. **59**(6), 3272–3277 (2012).
[100]A. S. Tremsin *et al.*, "Neutron resonance transmission spectroscopy with high spatial and energy resolution at the J-PARC pulsed neutron source," Nucl. Instrum. Methods Phys. Res., Sect. A **746**, 47–58 (2014).
[101]A. S. Tremsin *et al.*, "Non-destructive studies of fuel pellets by neutron resonance absorption radiography and thermal neutron radiography," J. Nucl. Mater. **440**(1-3), 633–646 (2013).
[102]Y. Zhang *et al.*, *Neutron Resonance Radiography and Application to Nuclear Fuel Materials* (Oak Ridge National Laboratory (ORNL), Oak Ridge, TN, 2018).
[103]K. Myhre *et al.*, *Nondestructive Examination of Uranium Oxide Kernels Using Energy-Resolved Neutron Imaging* (Oak Ridge National Laboratory (ORNL), Oak Ridge, TN, 2019).
[104]T. Shinohara *et al.*, "The energy-resolved neutron imaging system, RADEN," Rev. Sci. Instrum. **91**(4), 043302 (2020).

[105]H. Bilheux *et al.*, "Overview of the conceptual design of the future VENUS neutron imaging beam line at the Spallation Neutron Source," in Proceedings of the 10th World Conference on Neutron Radiography (Wcnr-10), 2015, pp. 55–59.
[106]M. Strobl, "The scope of the imaging instrument project ODIN at ESS," Phys. Procedia **69**, 18–26 (2015).
[107]M. Morgano, E. Lehmann, and M. Strobl, "Detectors requirements for the ODIN beamline at ESS," Phys. Procedia **69**, 152–160 (2015).
[108]J. Chen *et al.*, "First neutron Bragg-edge imaging experimental results at CSNS," Chin. Phys. B **30**(9), 096106 (2021).
[109]P. Adams *et al.*, *First Experiments: New Science Opportunities at the Spallation Neutron Source Second Target Station (Abridged)* (Oak Ridge National Laboratory (ORNL), Oak Ridge, TN, 2020).
[110]A. Momose *et al.*, "Recent progress in X-ray and neutron phase imaging with gratings," Quant. Beam Sci. **4**(1), 9 (2020).
[111]L. Crow *et al.*, "The CG1 instrument development test station at the high flux isotope reactor," Nucl. Instrum. Methods Phys. Res., Sect. A **634**, S71–S74 (2011).
[112]L. Santodonato *et al.*, "The CG-1D neutron imaging beamline at the Oak Ridge National Laboratory high flux isotope reactor," in Proceedings of the 10th World Conference on Neutron Radiography (Wcnr-10), 2015, pp. 104–108.
[113]T. Kamiyama *et al.*, "Structural change of carbon anode in a lithium-ion battery product associated with charging process observed by neutron transmission Bragg-edge imaging," Phys. Procedia **88**, 27–33 (2017).
[114]K. Kino *et al.*, "Two-dimensional imaging of charge/discharge by Bragg edge analysis of electrode materials for pulsed neutron-beam transmission spectra of a Li-ion battery," Solid State Ion. **288**, 257–261 (2016).
[115]K. Kino *et al.*, "First imaging experiment of a lithium ion battery by a pulsed neutron beam at J-PARC/MLF/BL09," Phys. Procedia **69**, 612–618 (2015).
[116]A. Steuwer *et al.*, "Bragg edge determination for accurate lattice parameter and elastic strain measurement," Phys. Status Solidi A **185**(2), 221–230 (2001), https://onlinelibrary.wiley.com/doi/abs/10.1002/1521-396X(200106)185:2%3C221::AID-PSSA221%3E3.0.CO;2-C
[117]A. J. Brooks *et al.*, "Porosity detection in electron beam-melted Ti-6Al-4V using high-resolution neutron imaging and grating-based interferometry," Prog. Addit. Manuf. **2**(3), 125–132 (2017).
[118]A. J. Brooks *et al.*, "Neutron interferometry detection of early crack formation caused by bending fatigue in additively manufactured SS316 dogbones," Mater. Des. **140**, 420–430 (2018).
[119]A. J. Brooks *et al.*, "Early detection of fracture failure in SLM AM tension testing with Talbot-Lau neutron interferometry," Addit. Manuf. **22**, 658–664 (2018).
[120]A. S. Tremsin *et al.*, "High-resolution strain mapping through time-of-flight neutron transmission diffraction with a microchannel plate neutron counting detector," Strain **48**(4), 296–305 (2012).
[121]R. Betti *et al.*, "Monitoring the structural health of main cables of suspension bridges," J. Civil Struct. Health Monit. **6**(3), 355–363 (2016).
[122]A. Brügger *et al.*, "Partitioning of clamping strains in a nineteen parallel wire strand," Exp. Mech. **57**(6), 921–937 (2017).
[123]A. J. Brooks *et al.*, "Intact, commercial lithium-polymer batteries: Spatially resolved grating-based interferometry imaging, Bragg edge imaging, and neutron diffraction," Appl. Sci. **12**(3), 1281 (2022).
[124]M. Strobl, "Future prospects of imaging at spallation neutron sources," Nucl. Instrum. Methods Phys. Res., Sect. A **604**(3), 646–652 (2009).
[125]J. R. Santisteban *et al.*, "Strain imaging by Bragg edge neutron transmission," Nucl. Instrum. Methods Phys. Res., Sect. A **481**(1-3), 765–768 (2002).
[126]T. Reimann *et al.*, "Neutron dark-field imaging of the domain distribution in the intermediate state of lead," J. Low Temper. Phys. **182**(3-4), 107–116 (2015).
[127]M. Strobl *et al.*, "Neutron dark-field tomography," Phys. Rev. Lett. **101**(12), 123902 (2008).
[128]S. Zabler, "Phase-contrast and dark-field imaging," J. Imag. **4**(10), 113 (2018).
[129]C. Grunzweig *et al.*, "Design, fabrication, and characterization of diffraction gratings for neutron phase contrast imaging," Rev. Sci. Instrum. **79**(5), 053703 (2008).
[130]A. S. Tremsin *et al.*, "High-resolution strain mapping through time-of-flight neutron transmission diffraction," in Mechanical Stress Evaluation by Neutrons and Synchrotron Radiation Vi (2014), Vol. 772, p. 9.
[131]J. M. LaManna *et al.*, "Improving material identification by combining X-ray and neutron tomography," in *Developments in X-Ray Tomography Xi*, 10391 (SPIE, 2017), pp. 20–26.
[132]M. Zambrano *et al.*, "Implementation of dynamic neutron radiography and integrated X-ray and neutron tomography in porous carbonate reservoir rocks," Front. Earth Sci. **7**, 329 (2019).
[133]D. Mannes *et al.*, "Combined neutron and X-ray imaging for non-invasive investigations of cultural heritage objects," Phys. Procedia **69**, 653–660 (2015).
[134]S. Haber-Pohlmeier *et al.*, "Combination of magnetic resonance imaging and neutron computed tomography for three-dimensional rhizosphere imaging," Vadose Zone J. **18**(1), 1–11 (2019).
[135]J. Y. Y. Lin *et al.*, "Recent developments of MCViNE and its applications at SNS," J. Phys. Commun. **3**(8), 085005 (2019).
[136]J. Y. Y. Lin *et al.*, "MCViNE–An object oriented Monte Carlo neutron ray tracing simulation package," Nucl. Instrum. Methods Phys. Res., Sect. A **810**, 86–99 (2016).
[137]P. K. Willendrup and K. Lefmann, "McStas (i): Introduction, use, and basic principles for ray-tracing simulations," J. Neutron Res. **22**(1), 1–16 (2020).
[138]P. K. Willendrup and K. Lefmann, "McStas (ii): An overview of components, their use, and advice for user contributions," J. Neutron Res. **23**(1), 7–27 (2021).
[139]K. Lefmann and K. Nielsen, "McStas, a general software package for neutron ray-tracing simulations," Neutron News **10**(3), 20–23 (1999).